Spatial disconnection between stellar and dust emissions: The test of the Antennae Galaxies (Arp 244)

L.-M. Seillé, V. Buat, W. Haddad, A. Boselli, M. Boquien, L. Ciesla, Y. Roehlly, D. Burgarella

A&A 665, A137 (2022)
https://doi.org/10.1051/0004-6361/202243702

Astronomy & Astrophysics

Spatial disconnection between stellar and dust emissions: The test of the Antennae Galaxies (Arp 244)

L.-M. Seillé[1], V. Buat[1,2], W. Haddad[1], A. Boselli[1], M. Boquien[3], L. Ciesla[1], Y. Roehlly[1], and D. Burgarella[1]

[1] Aix Marseille Univ, CNRS, CNES, LAM, Marseille, France
e-mail: lise-marie.seille@lam.fr
[2] Institut Universitaire de France (IUF), Paris, France
e-mail: veronique.buat@lam.fr
[3] Centro de Astronomía (CITEVA), Universidad de Antofagasta, Avenida Angamos 601, Antofagasta, Chile

Received 3 April 2022 / Accepted 15 July 2022

ABSTRACT

Context. The detection of dust-rich high-redshift galaxies with the Atacama Large Millimeter Array (ALMA), the cold dust emission of which is spatially disconnected from the ultraviolet emission, bears a challenge for modelling their spectral energy distributions (SEDs) with codes based on an energy budget between the stellar and dust components.
Aims. We want to test the validity of energy balance modelling on a nearby resolved galaxy with vastly different ultraviolet and infrared spatial distributions and to decipher the kinds of information that can be reliably retrieved from the analysis of the full SED.
Methods. We used 15 broadband images of the Antennae Galaxies ranging from far-ultraviolet to far-infrared and divided Arp 244 into 58 square ∼1 kpc^2 regions. We fit the data with CIGALE to determine the star formation rate, stellar mass, and dust attenuation of each region. We compared these quantities to those obtained for Arp 244 as a whole.
Results. The SEDs of the 58 regions and Arp 244 are well fitted. The estimates of the star formation rate and stellar mass for the whole galaxy are found to be consistent – within one sigma – with the same parameters summed over the 58 regions. We present the spatial distribution of these physical parameters as well as the shape of the attenuation curve across the Antennae Galaxies. We find that the Overlap Region exhibits a high star formation rate, attenuation, and a shallow attenuation curve. We observe a flattening of the attenuation curves with increasing attenuation and dust surface density in agreement with the predictions of hydrodynamical simulations coupled with radiative transfer modelling.

Key words. galaxies: ISM – galaxies: star formation – galaxies: high-redshift – galaxies: individual: Arp 244

1. Introduction

Modelling and fitting the spectral energy distributions (SEDs) of galaxies is one of the most popular methods for deriving the physical parameters that are crucial for the study of galaxy evolution, such as the star formation rate (SFR) and the stellar mass. However, dust can drastically change the shape of the ultraviolet (UV) to near-infrared (NIR) SED as it absorbs and scatters photons, mostly at wavelengths shorter than 1 μm, and thermally emits the absorbed energy in the infrared (IR; from ∼3 to ∼1000 μm). Physically based SED modelling codes take this effect into account by applying the energy balance principle: the energy radiated by dust corresponds to the energy of the absorbed stellar light (e.g., da Cunha et al. 2008; Noll et al. 2009; Carnall et al. 2018; Boquien et al. 2019). SED-fitting codes introduce an attenuation recipe to redden the stellar continuum. This mostly consists of the attenuation curve measured for starburst galaxies (Calzetti et al. 2000) or of the recipe of Charlot & Fall (2000) with a power-law dependence of the effective attenuation on wavelength and a differential amount of attenuation for young and older stars.

Variations in attenuation laws in local and distant galaxies have been observed (e.g., Kriek & Conroy 2013; Buat et al. 2012; Battisti et al. 2017; Salim et al. 2018; Boquien et al. 2022; Lo Faro et al. 2017, LF17 hereafter). The attenuation law is found to flatten out when the attenuation increases (e.g., Salmon et al. 2016; Buat et al. 2018; Boquien et al. 2022). Radiation transfer models applied to simple geometries (Chevallard et al. 2013) or to hydrodynamical simulations (Roebuck et al. 2019; Trayford et al. 2020) also predict similar trends. Both observational and theoretical studies lead to the conclusion that a single attenuation curve does not account for all star-forming galaxies and that more flexible curves are required (Salim & Narayanan 2020).

Recent observations of high-redshift massive dusty galaxies with the Atacama Large Millimeter Array (ALMA) found a very compact dust emission, and a clumpy rest-frame UV emission distributed in clumps located far away from the compact dust emission (e.g., Elbaz et al. 2018; Rujopakarn et al. 2019). These very different dust and stellar distributions raise the question of the validity of a local energy balance which is nevertheless still expected to be valid at a global scale. The energy balance linking stellar and dust emissions is expected to have an impact on the physical parameters derived from the modelling of the global emission. This may be at least partially reflected by the variable effective attenuation curve as shown in Buat et al. (2019).

In this paper, we use NGC 4038/NGC 4039 (also known as Arp244 or the Antennae Galaxies) as a proxy to test the accuracy of SED modelling techniques based on energy conservation in high-redshift dusty galaxies with very complex geometry (e.g., Dunlop et al. 2017; Elbaz et al. 2018). The Antennae Galaxies are a pair of interacting galaxies in their second encounter (Zhang et al. 2010), although Privon et al. (2013) suggest that Arp 244 is at a slightly earlier stage in its merging process. The

Table 1. Characteristics of the filters used for the study.

Filters	$\lambda_{\rm eff}$ (μm)	Bandwidth (μm)	Processed Pixel Size	Minimum S/N
FUV	0.155	0.134–0.181	1.5″	7.3
NUV	0.230	0.169–0.301	1.5″	6.4
PS *g*	0.481	0.394–0.559	0.25″	4.0
PS *r*	0.616	0.539–0.704	0.25″	5.6
PS *i*	0.750	0.678–0.830	0.25″	5.4
PS *z*	0.867	0.803–0.935	0.25″	5.3
PS *y*	0.961	0.910–1.08	0.25″	5.7
VISTA *Ks*	2.14	1.93–2.37	0.34″	4.3
IRAC 1	3.51	3.13–3.96	0.6″	6.0
IRAC 2	4.44	3.92–5.07	0.6″	3.0
IRAC 3	5.63	4.90–6.51	0.6″	6.6
IRAC 4	7.59	6.30–9.59	0.6″	5.5
MIPS 1	23.2	19.9–30.9	1.5″	7.0
PACS 70	68.9	55.7–97.7	1.4″	8.8
PACS 160	153.9	117.8–243.6	2.85″	9.0

pair are currently going through a starburst phase in which the collision of clouds of gas and dust causes rapid star formation. Their proximity of 21 Mpc (Riess et al. 2011) allows a multi-wavelength UV to far-IR (FIR) study at kiloparsec (kpc) scale. Arp 244 exhibits very different UV and FIR spatial distributions, which are akin to the dusty high-redshift galaxies observed with ALMA. Our estimation of the distance between the regions of intense UV and FIR emissions is ≃7 kpc in Arp 244 which can be considered as typical in dusty high-redshift star-forming galaxies (e.g., Rujopakarn et al. 2016, 2019; Hodge et al. 2016; Gómez-Guijarro et al. 2018). This makes the Antennae Galaxies very good candidates for the investigation of the reliability of both global and local (kpc scale) measurements of physical quantities.

The paper is structured as follows: in Sect. 2, we introduce the multi-band data that we use in this study, and describe the multi-wavelength photometry of individual regions. Section 3 is dedicated to the SEDs modules. We present our results in Sect. 4 and discuss them in Sect. 5. Conclusions are given in Sect. 6.

2. Photometry

2.1. Multi-wavelength images

We retrieved images of the Antennae Galaxies from the UV to the FIR. Both FUV (1516 Å) and NUV (2267 Å) images come from the GALEX Ultraviolet Atlas of Nearby Galaxies distributed by Gil de Paz et al. (2007). The images in the *g*, *r*, *i*, *z*, and *y* bands are obtained from the Pan-STARRS DR2 survey catalogue (Chambers et al. 2016). The VISTA *Ks* image obtained during the VHS survey by McMahon et al. (2013) was retrieved from the ESO Science Archive Facility. The *Spitzer* data consists of the four InfraRed Array Camera (IRAC, Fazio et al. 2004) bands and the 24 μm band from the Multiband Imaging Photometer for *Spitzer* (MIPS, Rieke et al. 2004). These images, processed by Bendo et al. (2012), were retrieved from the *Spitzer* Heritage Archive. We obtained user-provided data products of the Photodetector Array Camera and Spectrometer (PACS, Klaas et al. 2010) 70 (PACS-blue) and 160 (PACS-red) μm maps from the *Herschel* (Pilbratt et al. 2010) Science Archive. We retrieved the PACS images processed with the program package Scanamorphos (Roussel 2013). The main characteristics of the filters used as well as the spatial resolution of the images and their minimum signal to noise ratios (S/Ns) are given in Table 1.

2.2. Region selection and photometric extraction

The images are all corrected for Galactic extinction using the Milky Way extinction curve of Cardelli et al. (1989) and the colour excess ($E(B-V) = 0.147$) from Schlafly & Finkbeiner (2011). All images are background-subtracted using the 2D background estimator *MedianBackground* from the *photutils.background* library in Python.

The images are degraded to the lowest resolution and pixel size of our data set which corresponds to the 160 μm image (resolution of 10.65″). This image is processed with Scanamorphos leading to a reduction in pixel size from 6.4″ on the detector to 2.85″ in the generated image. We convolve all the other images to reach this resolution using the 2D Gaussian kernel from the Python *astropy.convolution* library.

All the images are then re-projected with the *reproject_interp* function from the *reproject* library in Python in order to fit the orientation of the PACS images. This function also ensures that all our images are of the same size as the 160 μm image. At the end of the full process, all the images have the same size, orientation, pixel size, and resolution. Fluxes are conserved throughout this process.

The images are then divided into square boxes of four 2.85″ × 2.85″ pixels, resulting in square areas of 1.3 kpc^2 (Fig. 1) which is consistent with the minimal size prescription for an unbiased SFR measurement by Kennicutt & Evans (2012). We refer to each square box as a 'region'.

We want to have a good coverage of Arp 244 and a high signal to noise ratio (S/N) in all bands. We define 58 regions with a S/N higher than 3 in all bands. The minimum S/N for each band is given in Table 1. The lowest one is for the IRAC2 band. We present a map of the 58 selected regions over-imposed on the 160 μm image in panel a of Fig. 2.

The flux uncertainties are estimated by considering the background noise and the calibration uncertainty. The background noise at each wavelength is computed as the mean of the flux of 66 regions located around the Antennae (see Appendix A for more details). The calibration uncertainties for the GALEX, IRAC, and MIPS images are taken from Zhang et al. (2010): 5% for FUV,

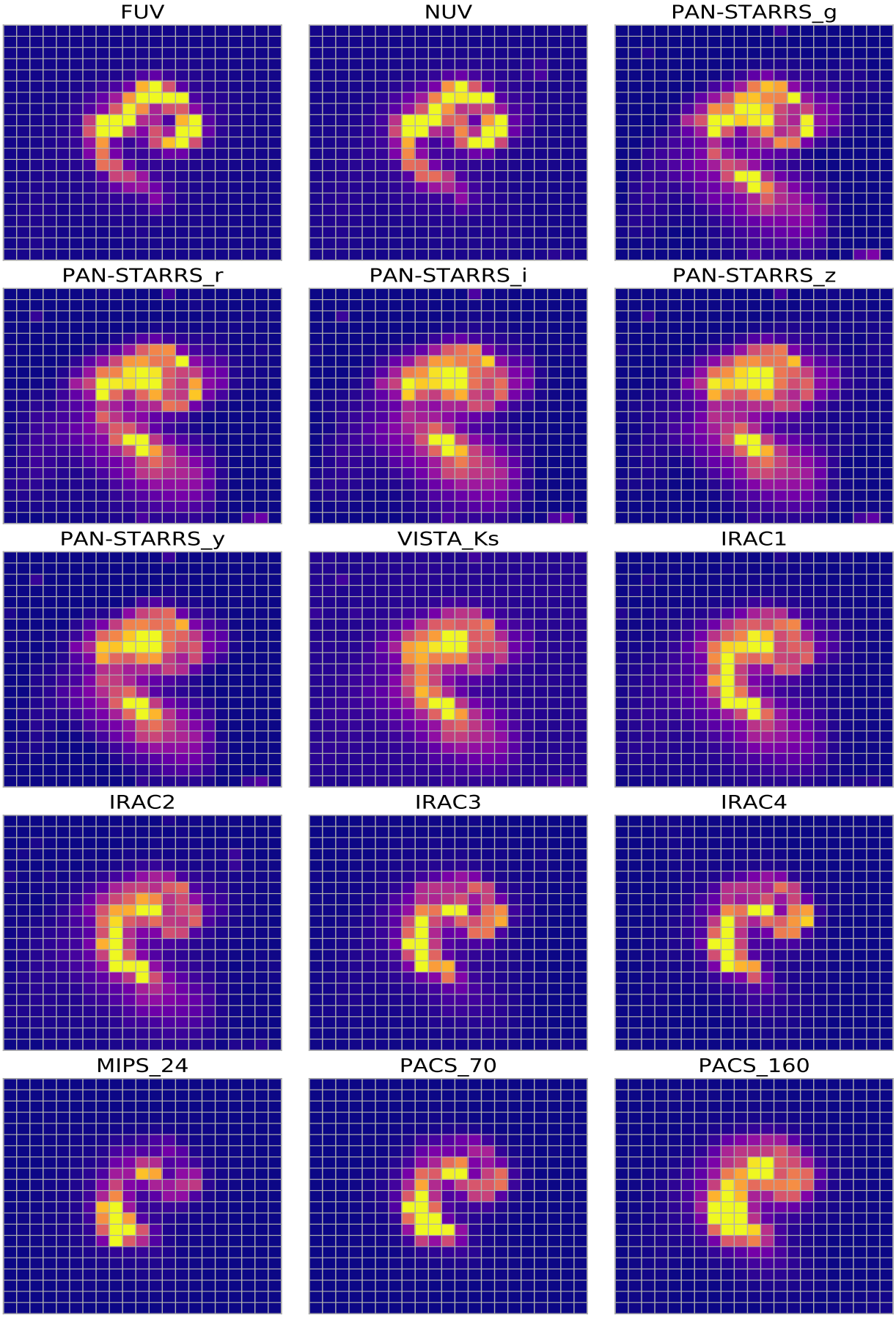

Fig. 1. Images of the Antennae galaxies in the 15 different bands downgraded to the resolution of the 160 μm image.

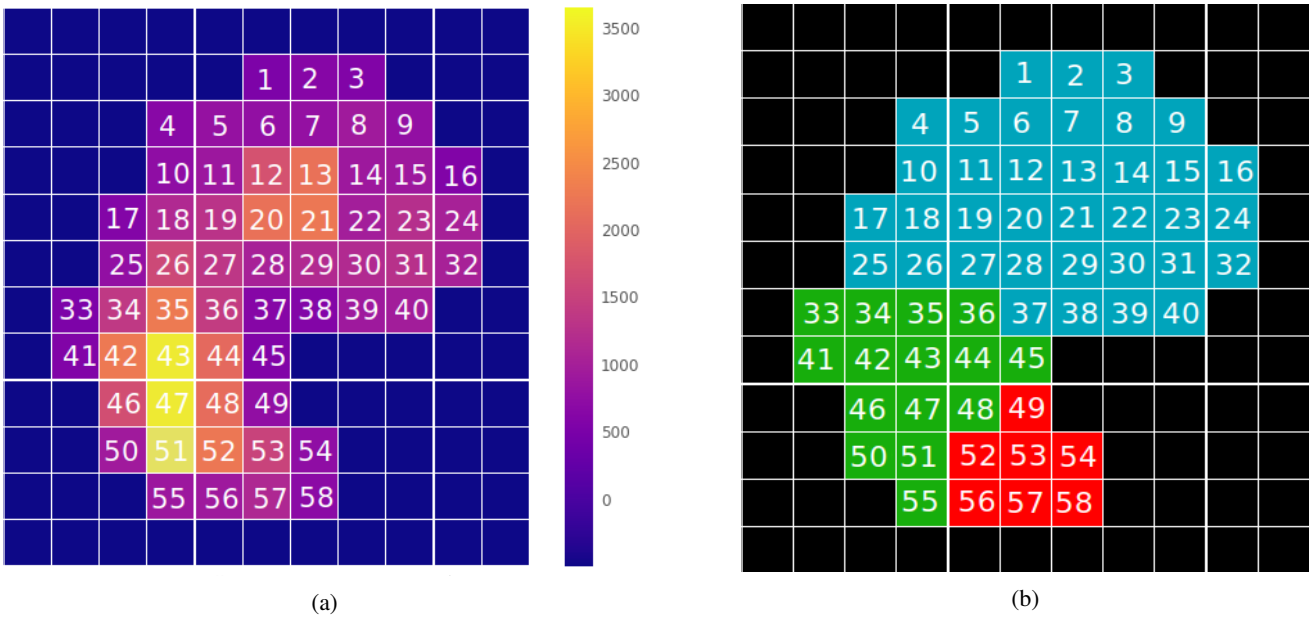

(a) (b)

Fig. 2. The 58 regions of the Antennae Galaxies in the 160 µm band. Each region is colour-coded with its flux in mJy (*panel a*). In *panel b*, we separate Arp 244 into its three main components: regions that are part of NGC4038 are colour coded in blue while the regions that are part of NGC 4039 are colour coded in red and regions in the Overlap are coloured in green.

3% for NUV, 10% for IRAC, and 4% for MIPS. The calibration uncertainty of the PACS images is set to 5% (Karl et al. 2013). The Pan-STARRS calibration uncertainty is taken equal to 5% instead of 1% given by Magnier et al. (2020). We choose to increase the uncertainty to avoid excessive inhomogeneity with the other bands. The flux uncertainty in the *Ks* band is dominated by the background noise and we estimate it to be 20%.

We identify the well-known broad regions of the Antennae Galaxies: NGC 4038, NGC 4039, and the Overlap Region. In panel (b) of Fig. 2, regions 1 to 32 and 37–40 correspond to NGC 4038, regions 49, 52–54 and 56–58 correspond to NGC 4039. The Overlap Region consists of regions 33–36, 41–48, 50, 51, and 55. We also identify the Western Arm, which is a part of NGC 4038, specifically regions 8, 15, 23, 24, 29–32, 39, and 40.

In the following sections, we analyse individual SEDs of the square regions (called 'SEDn', n being the region number) and the integrated SED corresponding to the sum of fluxes over the 58 regions (referred to as the integrated SED).

3. Spectral energy distribution fitting

To fit the SEDs, we use the modelling software CIGALE[1]. For a complete description of CIGALE and its functionalities; see Boquien et al. (2019). The models are built by successively calling modules, each corresponding to a single physical component or process. CIGALE combines a UV to NIR stellar SED with a dust component emitting in the IR and conserves the energy balance between stellar dust absorption and dust re-emission. The nebular emission is added from the Lyman continuum photons produced by the stellar emission in photodissociation regions. The continuum nebular emission and the emission lines are calculated from a grid of nebular templates (Villa-Vélez et al. 2021). The quality of the fit is assessed by the value of the χ^2 and the value of the physical parameters and their corresponding uncertainties are estimated as the likelihood-weighted means and standard deviations. Below, we briefly present the modules we use and the input parameter values.

[1] https://cigale.lam.fr/version-2020.0/

3.1. CIGALE modules

3.1.1. Star formation history and stellar populations

First we define a star formation history (SFH) and the single stellar population (SSP) model to compute the stellar emission spectrum. We use a delayed exponential SFH described as

$$\mathrm{SFR} \propto t \times \exp(-t/\tau_{\mathrm{main}}), \quad (1)$$

where τ_{main} is the e-folding time. The module allows the addition of an optional burst to the existing delayed exponential. The simulations of the merger of the Antennae Galaxies performed by Karl et al. (2010) give an age of burst of ~40 Myr after the second encounter. Therefore, we define a burst of constant star formation with an age (age_{burst}) fixed to 40 Myr (see Sect. 3.3 for more details). The amplitude of the burst is measured with the fraction of stellar mass produced in the burst, f_{burst}. We refer to the age of the onset of star formation as age_{main} and we fix it to 12 Gyr (fixing it to 13 Gyr would not change our results). The e-folding time of the main population, τ_{main}, as well as f_{burst} are free parameters. We use the SSP models of Bruzual & Charlot (2003) and the initial mass function (IMF) of Chabrier (2003) and we fix the metallicity to the solar value. All the input values are summarised in Table 2.

3.1.2. Dust attenuation and emission

To compute the dust attenuation, we choose a module based on the Charlot & Fall (2000; hereafter CF00) model. The key feature of this model is the computation of two different attenuations, one for the birth clouds (BCs) and one for the interstellar medium (ISM). In this way, we are able to properly account for an age-dependent attenuation where not only the total amount of dust attenuation changes as a function of the stellar age but

Table 2. CIGALE modules and input parameters used for all the fits.

Parameter	Symbol	Range
Delayed SFH		
Age of the main population	$age_{\rm main}$	12 000
e-folding timescale of the delayed SFH	$\tau_{\rm main}$	1000–8000
Age of the burst	$age_{\rm burst}$	40
Burst stellar mass fraction	$f_{\rm burst}$	0–0.1
Stellar populations synthesis		
Initial mass function	IMF	Chabrier
Metallicity	Z	0.02
Dust attenuation		
V-band attenuation in the ISM	$A_{\rm V}^{\rm ISM}$	0.1–3.5
$A_{\rm V}^{\rm ISM}/(A_{\rm V}^{\rm ISM}+A_{\rm V}^{\rm BC})$	μ	0.5
Power-law slope of dust attenuation in the BCs	$n^{\rm BC}$	0.7
Power-law slope of dust attenuation in the ISM	$n^{\rm ISM}$	0–1.2
Dust emission		
Mass fraction of PAHs	$q_{\rm PAH}$	0.47–5.95
Minimum radiation field	$U_{\rm min}$	1.0–15.0
Power-law slope of the radiation field	α	2.0
Fraction illuminated	γ	0.001–0.05

also the way the stellar light is extinguished, as originally introduced by CF00. We use a modified version of CF00, in which two different power-law attenuation curves are used to compute the total attenuation:

$$A_\lambda^{\rm BC} = A_{\rm V}^{\rm BC}(\lambda/0.55)^{n^{\rm BC}},$$
$$A_\lambda^{\rm ISM} = A_{\rm V}^{\rm ISM}(\lambda/0.55)^{n^{\rm ISM}}, \quad (2)$$

where $n^{\rm ISM}$ is the slope of the attenuation curve for the ISM and $n^{\rm BC}$ the slope of the attenuation curve for the birth clouds. This latter is fixed to a reference value of −0.7 (Charlot & Fall 2000; Lo Faro et al. 2017). The power-law exponent of the variation of the effective attenuation in the ISM, $n^{\rm ISM}$, is also fixed to −0.7 in the original recipe of CF00. However, we decided to treat it as a free parameter in our analysis because it has been shown to vary among galaxies (e.g., Buat et al. 2012; Chevallard et al. 2013; Kriek & Conroy 2013; Battisti et al. 2017; Lo Faro et al. 2017; Salim et al. 2018; Trayford et al. 2020; Pantoni et al. 2021; Boquien et al. 2022). The V-band attenuation in the ISM, $A_{\rm V}^{\rm ISM}$, is also a free parameter. The attenuation for the birth clouds, $A_{\rm V}^{\rm BC}$, is computed using the μ parameter:

$$\mu = \frac{A_{\rm V}^{\rm ISM}}{A_{\rm V}^{\rm ISM}+A_{\rm V}^{\rm BC}}. \quad (3)$$

The age threshold for the separation between young stars (still attenuated by birth clouds) and older stars (only attenuated by the ISM) is 10 Myr.

To model the dust emission, we use the models from Draine & Li (2007) and updated in Draine et al. (2014). The model is built as follows: a fraction $(1-\gamma)$ of the dust mass is heated by a starlight intensity $U_{\rm min}$, while the remaining fraction γ is exposed to starlight with intensities $U_{\rm min} < U < U_{\rm max}$, with a power-law distribution $\mathrm{d}M/\mathrm{d}U \propto U^{-\alpha}$. The polycyclic aromatic hydrocarbon (PAH) abundance, $q_{\rm PAH}$, is also a free parameter in the models. As suggested by Draine et al. (2014), we fix $U_{\rm max}$ to 10^7 and the slope of the power law, α, to 2. The shape of the dust-emission spectrum is then determined by three free parameters: $q_{\rm PAH}$, $U_{\rm min}$, and γ. Table 2 provides all the input values.

3.2. Fitting the broadband SEDs

The median of the reduced χ^2 for our 58 regions is 0.65 with a minimum of 0.27 and a maximum of 2.19. Each fit is checked individually to ensure that our sample is well fitted overall. However, the values and uncertainties of the physical parameters used in this study are estimated from their probability distribution function which accounts for the likelihood of each model. We present the integrated SED of the Antennae Galaxies in Fig. 3 and the SEDs of two regions in Fig. 4. The IR luminosity of Arp 244 is $8\times10^{10}\,L_\odot$, the SFR is at 8.5 $M_\odot\,{\rm yr}^{-1}$, and the stellar mass is $4.5\times10^{10}\,M_\odot$.

Depending on the region considered, the SEDs can exhibit completely different features. We illustrate these contrasted situations in Fig. 4 with two very different environments: a region of the nucleus of NGC 4038 (region 20) and a region that is part of the Overlap between the two galaxies (region 47). Two features stand out while comparing these two SEDs: the high intrinsic emission in the UV band and the higher emission in both PACS bands for region 47 compared to region 20. As part of the nucleus of a galaxy that was previously a spiral galaxy, region 20 is found to have a low SFR (0.18 $M_\odot\,{\rm yr}^{-1}$) while region 47 has the second highest SFR of the study (0.51 $M_\odot\,{\rm yr}^{-1}$).

The Overlap Region hosts numerous star-forming regions (Whitmore & Schweizer 1995), leading to the observed level of intrinsic UV emission in region 47. A large fraction of the UV light emitted is absorbed by dust ($A_{\rm FUV} = 3.4\pm0.2$ mag) – as shown in the SED – and is re-emitted in the IR. In region 20, this effect still occurs but on a lower level ($A_{\rm FUV} = 2.6\pm0.2$ mag).

3.3. Mock analysis and parameter determination

Before discussing the estimates of the physical parameters in detail in Sect. 4, we want to check the validity and accuracy of our estimates through the mock analysis described below.

With CIGALE we can generate catalogues of artificial sources for which the physical parameters are known (Buat et al. 2014; Ciesla et al. 2015). To build the mock catalogue, CIGALE uses the best-fit model of each of the objects previously obtained

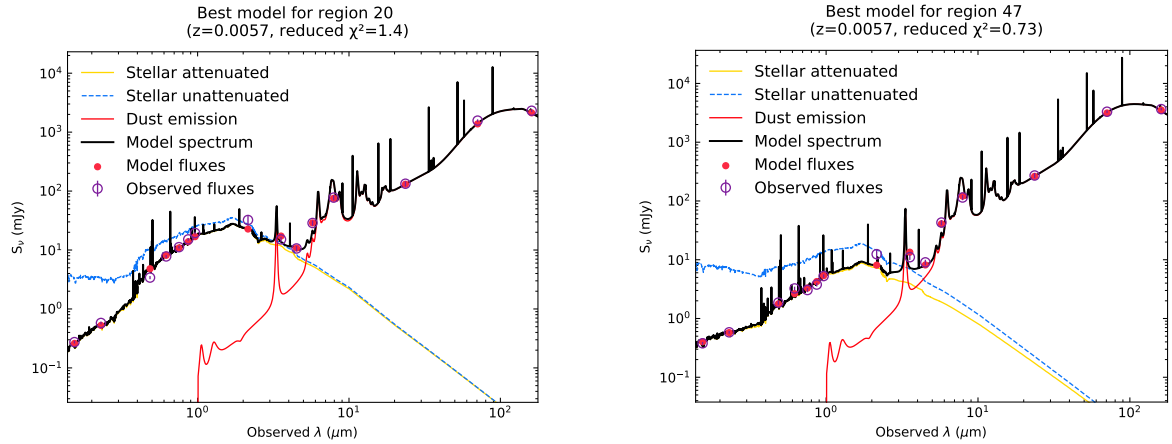

Fig. 3. Comparison of the SEDs from a region of the nucleus of NGC4038 (*left panel*) and a region that is part of the Overlap (*right panel*).

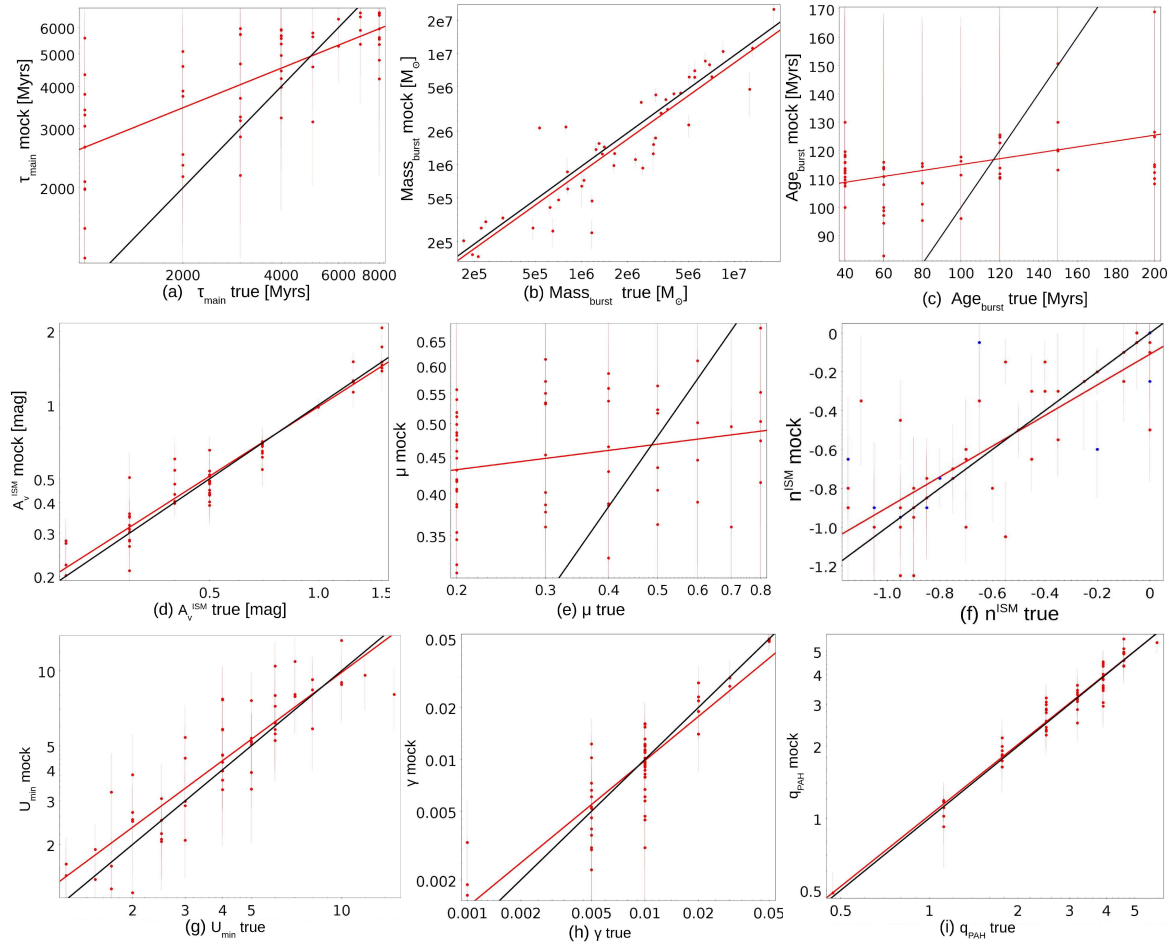

Fig. 4. Results of the mock analysis. The input parameters used to build the mock catalogue are shown on the *x*-axis while the results of the fitting of the mock catalogues are shown on the *y*-axis with their associated error bars. The black solid line indicates the one-to-one relationship. The red solid line represents the linear fit of our points. The blue dots in *panel f* are the regions with $A_{\rm V}^{\rm ISM} < 0.3$ mag.

through our SED-fitting procedure. The flux densities of the mock SEDs are computed by randomly picking a flux value from the normal distribution generated using the best model flux as the mean value and the photometric error as the standard deviation. CIGALE is then run on this artificial catalogue with the same configuration as for the first run in order to compare the exact values of the physical parameters corresponding to the artificial SEDs to the parameters estimated by the code with the probability density function of each parameter. The analysis consists in comparing the results of the Bayesian-like analysis of this mock catalogue provided by CIGALE with the input parameters from the best models.

We use this test to check the robustness of the output SED-fitting parameters of interest for our study and our ability to constrain them. We are mostly interested in studying the parameters linked to star formation and attenuation as the latter is critical

in a dust-obscured object such as the Antennae Galaxies. Below, we describe each free parameter individually, its robustness, and the need for a more in-depth discussion in the following sections.

The first parameter is $\tau_{\rm main}$, the e-folding time of the main population. As seen in Fig. 5, panel a, the comparison between the true value and its estimation based on mock catalogues suggests that this parameter is not well constrained, with only a loose trend between the two quantities. We decided to keep it as a free parameter to introduce some flexibility in the fits but we do not discuss the values of this parameter.

We define the stellar mass produced during the burst, $\rm Mass_{burst}$, as the product of the Bayesian estimation of $f_{\rm burst}$ and of the total stellar mass. $f_{\rm burst}$ is varying from 0 (no recent burst) to 0.05 (5% of the stellar mass formed during the last 40 Myr). $\rm Mass_{burst}$ is well constrained (Fig. 5, panel b), and so we keep $f_{\rm burst}$ as a free parameter.

In panel c of Fig. 5, we can see that the $\rm age_{burst}$ parameter is not constrained, and therefore we decided to fix it. Several ages of encounter are quoted in the literature: for example, 6 Myr after second pericenter passage (Renaud et al. 2015), 40 Myr after the second passage (Karl et al. 2010), and various stages just before or after the second passage (Privon et al. 2013). In our study, the most recent SFH in traced by the FUV emission which is only sensitive to timescales of several tens of millions of years (Boquien et al. 2014), and therefore we decided to fix $\rm age_{burst}$ to 40 Myr.

The input parameter quantifying the attenuation in the ISM, $A_{\rm V}^{\rm ISM}$, is well constrained (Fig. 5, panel d). In the following sections, we focus more on $A_{\rm V}$, which is the effective attenuation in the V-band. As μ is fixed (see below), and $A_{\rm V}$ is strongly correlated to $A_{\rm V}^{\rm ISM}$: indeed the average ratio of $A_{\rm V}/A_{\rm V}^{\rm ISM}$ is 1.1 which makes the solid constraint on $A_{\rm V}^{\rm ISM}$ also valid for $A_{\rm V}$.

The μ parameter which defines the effective attenuation in the birth clouds (EQ 3) is not constrained (Fig. 5, panel e). As we do not trace the very young stars, the lack of constraint on μ is expected, and so we decided to fix μ to a reference value of 0.5 (Małek et al. 2018). We checked that there is no noticeable difference in the attenuation, SFR, and the stellar mass between a run with fixed μ and a run where μ is free to vary. As a side note, Battisti et al. (2020) used a free μ and fixed power-law exponents in their work to account for a variable attenuation in the birth clouds.

The slope of the attenuation curve for the birth clouds was fixed to a reference value of −0.7 (Charlot & Fall 2000). The power-law exponent of the variation of the effective attenuation in the ISM, $n^{\rm ISM}$, is a free parameter in our analysis and it has been shown to vary among galaxies (e.g., Chevallard et al. 2013; Trayford et al. 2020; Pantoni et al. 2021). As pointed out by Corre et al. (2018), the slope of the attenuation cannot be accurately estimated if the amount of dust is too low. We therefore chose not to consider regions with a value of $A_{\rm V}^{\rm ISM}$ under 0.3 mag in our analysis of $n^{\rm ISM}$ but to keep them for the comparison in Sect 4.3. In panel f of Fig. 5, we see that, despite the relatively high uncertainties on the estimation of this parameter, there is a clear correlation between the true and estimated values. The parameters describing the dust emission, $U_{\rm min}$, γ and $q_{\rm PAH}$, are globally constrained (Fig. 5, panels g–i, respectively), and so we keep them as free parameters.

4. Physical parameter estimations

In this section, we present and discuss the spatial distribution of the parameters considered as well-constrained in the previous section. We begin with quantities related to the SFH followed by the parameters linked to dust. We conclude this section by focusing on the SFR, the stellar mass, and a comparison between estimates of the aforementioned parameters for the whole system and the ones obtained from the sum of the 58 regions.

4.1. SFH parameters

First, we focus on the analysis of the parameters of the SFH and their variation across the galaxies. Arp 244 is experiencing a merging event with a complex morphology and mass distribution. We present a pixelated map of the Antennae (Fig. 6, panel a) where each region is colour coded according to its value of $\rm Mass_{burst}$. Two components stand out with their high values: the Overlap Region and the Western Arm (defined in Sect. 2.2). Zhang et al. (2010) also find that the regions of the Western Arm exhibit a significant bursting population. This would suggest that the Western Arm was an efficient star-forming region in the past but its dusty star-forming regions have already dissipated as we are able to observe them clearly in the UV bands.

The bottom part of the Overlap Region is actively forming stars and we also notice regions in the far-right part of the Western Arm (Fig. 6, panel e) with a SFR of 1σ above the average. We identify region 51 as the MIR 'hotspot' described by Mirabel et al. (1998) because of its very high SFR ($0.45\,M_{\odot}\,{\rm yr}^{-1}\,{\rm kpc}^{-2}$).

The nuclei of NGC 4038 (regions 20 and 21) and NGC 4039 (regions 52 and 57) stand out with the highest stellar masses. As can be seen in panel f of Fig. 6, the Overlap Region acts as a bridge between NGC 4038 and NGC 4039 with a stellar mass comparable to that of regions surrounding both nuclei. This shows a clear disruption in the spatial distribution of the stellar mass in these galaxies.

4.2. Attenuation and dust emission

The distribution of the attenuation in the V-band $A_{\rm V}$ is presented in panel b of Fig. 6. The Overlap Region clearly stands out due to the high ratio of IR to UV emission coming from the high attenuation levels.

As can be seen in panel c of Fig. 6, $n^{\rm ISM}$ is much smaller than −0.7 in the Overlap Region and in NCG 4038, except for its outskirts, leading to flatter attenuation curves than the reference value of CF00. On the other hand, the nuclei of both progenitor galaxies have high negative values, indicating steeper attenuation curves than the reference value of CF00. We notice a tendency for regions with high attenuation to also have a shallower attenuation curve in the ISM (for a more in-depth discussion; see Sect. 5).

We notice the same pattern in the maps of the SFR and the mass of the bursting population: the Overlap Region and the Western Arm both exhibit above-average values. While the Overlap Region stands out in the attenuation map, the Western Arm has attenuation values comparable to the rest of NGC 4038. As the dusty star-forming regions in the Overlap Region have not dissipated yet, the total attenuation is much more efficient than in any part of Arp 244.

Regarding the PAH levels (Fig. 6, panel d), we see a homogeneous spatial distribution with two notable exceptions: the nucleus of NGC 4038 and the bottom part of the Overlap Region. The latter can be explained by the fact that PAHs are destroyed by UV radiation coming from star formation (e.g., Allain et al. 1996; Boselli et al. 2004), which is very intense in this part of

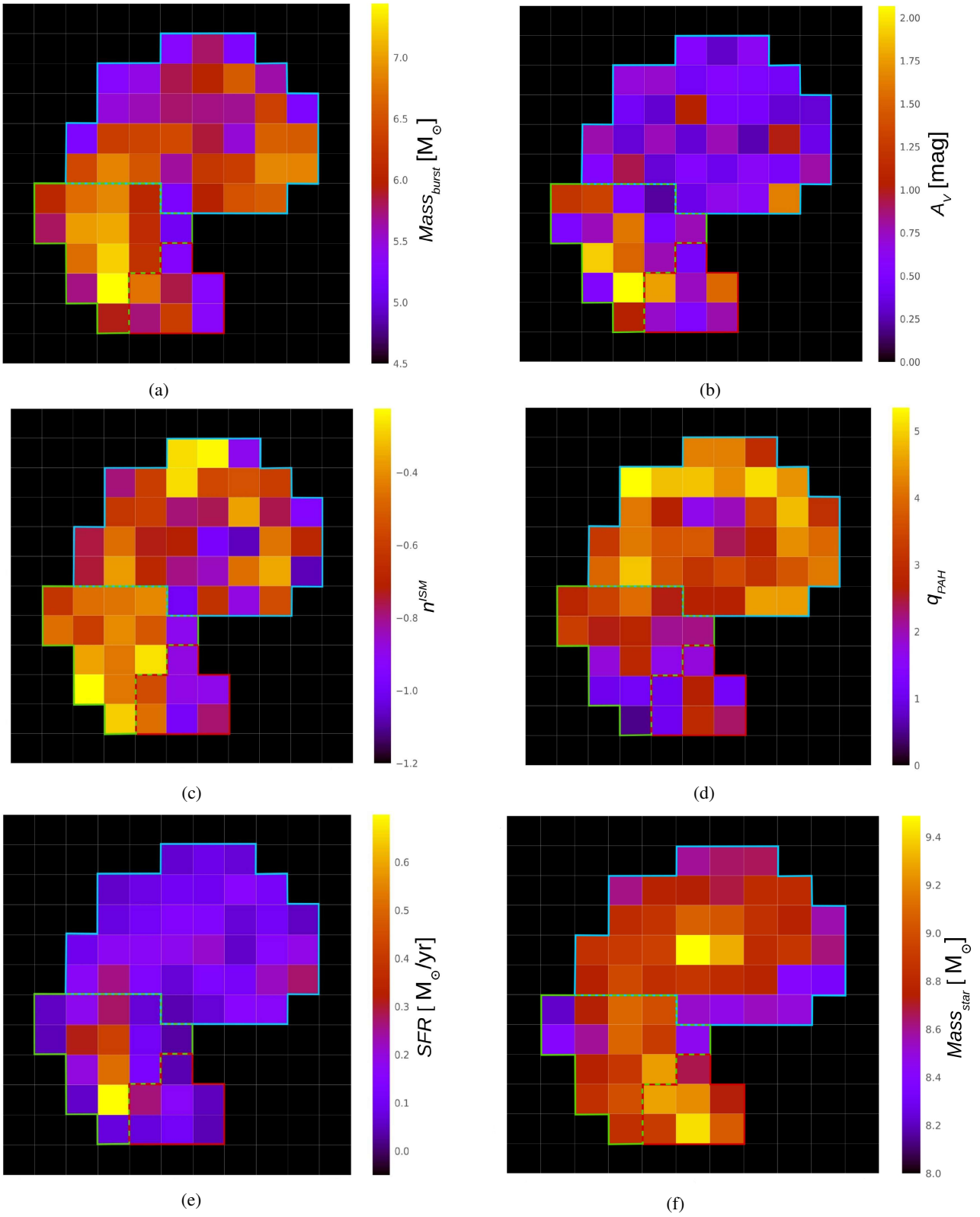

Fig. 5. Pixelated maps of the Antennae galaxies representing the spatial distribution of several parameters: (*a*) mass of the bursting population, (*b*) *V*-band attenuation, (*c*) slope of the attenuation curve, (*d*) $q_{\rm PAH}$ distribution, (*e*) star formation rate, and (*f*) stellar mass. Coloured contours are over-plotted to separate the three components of the galaxies: blue for NGC 4038, red for NGC 4039, and green for the Overlap. Logarithmic masses have been mapped in panels (*a*) and (*f*) to allow for better visualisation.

the galaxy. Both of these features, as well as the highest values of $q_{\rm PAH}$ in the northern part of NGC 4038, are in agreement with the distribution of PAH levels found by Zhang et al. (2010 and references therein).

Table 3. Comparison of the estimation of the physical parameters.

Parameter	Mean (1σ) [min, max]	58 fluxes added (1σ)
Mass of the bursting population ($10^7\ M_\odot$)	17.04 ($\pm$4.50) [0.01, 2.76]	12.05 ($\pm$2.42)
V-band attenuation	0.73 ($\pm$0.08) [0.23, 2.07]	0.68 ($\pm$0.10)
Power law slope of dust attenuation in the ISM	-0.62 ($\mp$0.25) [-1.07, -0.22]	-0.70 ($\mp$0.22)
PAH fraction	3.16 ($\pm$0.46) [0.49, 5.35]	2.86 ($\pm$0.58)
Star formation rate ($M_\odot\ \mathrm{yr}^{-1}$)	8.50 ($\pm$1.01) [0.03, 0.70]	8.21 ($\pm$1.53)
Stellar mass ($10^9\ M_\odot$)	45.8 ($\pm$13.0) [0.2, 3.1]	40.5 ($\pm$9.5)

Notes. The values of the SFR, stellar mass, and mass of the bursting population of the 58 regions in the second column are added together to allow for a comparison with integrated values. Thus, the minimum and maximum of these parameters correspond to the lowest and highest values out of the 58 regions.

4.3. Comparison of SFH and dust-related estimates of 58 regions versus integrated estimates

Here we compare the estimation of the parameters discussed above (SFR, stellar mass, mass of the bursting population, attenuation of the ISM in the V-band, and the slope of its curve) when the values obtained for the 58 regions are added together or when the whole system is fitted as a single source (Table 3).

Despite each single derived parameter spanning a wide range of values in the individual 58 regions because of the very perturbed nature of the Antennae, their mean or the sum of their values is in agreement with that derived for the whole system.

As the SFR in CIGALE is computed from the total IR luminosity, we compare our value of $\log(L_{\mathrm{IR}}) = 10.89$ to the one quoted by Sanders et al. (2003) in the IRAS sample catalogue: $\log(L_{\mathrm{IR}}) = 10.84$. Both values are close, meaning that our SFR are in agreement with the literature.

Our stellar mass estimates are only half of the value used by Karl et al. (2010) and Lahén et al. (2018) to reproduce an Antennae-like system. Part of this difference may be the result of the exclusion of the tails and outer regions of the system from our computations.

Both estimates of $A_{\mathrm{V}}^{\mathrm{ISM}}$ and n^{ISM} are within the error margin. Despite hosting widely different environments, the overall attenuation and its slope are still well recovered when fitting the entire system.

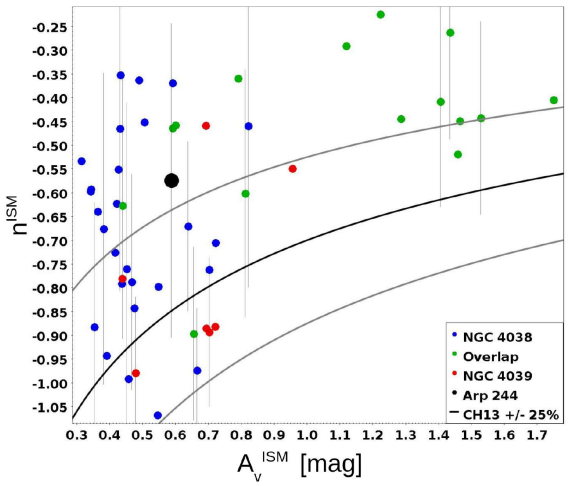

Fig. 6. Slope of the attenuation curve n^{ISM} plotted against the optical dust attenuation of the ISM, $A_{\mathrm{V}}^{\mathrm{ISM}}$. Blue, green, and red dots represent the 58 regions and the black dot the entire galaxy. Only one out of three error bars is plotted to maintain the readability of the plot. The black curve represents the best fit with their associated error (grey curves, defined as 25% by CH13).

5. Discussion

In this section, we compare our results on Arp 244 to several studies of dusty high-redshift galaxies and to the predictions of radiation transfer modelling in various galactic environments.

5.1. Comparison with observed dusty galaxies

Lo Faro et al. (2017) fitted a sample of $z \sim 2$ (ultra) luminous infrared galaxies (U)LIRGs with CIGALE. They obtained a mean power-law exponent $n^{\mathrm{ISM}} = -0.48$ (n^{BC} was fixed to -0.7). The authors also fitted nearby (U)LIRGs and found that these objects are again best fitted with a greyer attenuation curve than CF00. They concluded that local and $z \sim 2$ (U)LIRGs are characterised by similar optical depth values and dust-clouded star-forming environments which can be responsible for similar shapes in the dust attenuation curves.

At redshift $z \sim 2$, the (U)LIRGs from Pantoni et al. (2021) have an average specific star formation rate (sSFR) of $3.1\,\mathrm{Gyr}^{-1}$ while the average for non-(U)LIRG objects is $2.2\,\mathrm{Gyr}^{-1}$ (Tasca et al. 2015). Arp 244 has an average sSFR of $0.2\,\mathrm{Gyr}^{-1}$ which is a typical value for galaxies at redshift $z < 0.7$ (Tasca et al. 2015). Despite sharing spatially disconnected stellar and dust emissions, this comparison shows that some properties of $z \sim 2$ (U)LIRGs and the Antennae Galaxies can be very different.

Regions with the highest sSFR and physical properties most similar to those of high-z galaxies are found in the Overlap Region. They are best fitted with greyer attenuation curves (with n^{ISM} between -0.22 and -0.63) than the reference value of CF00 (-0.7). However, the value of n^{ISM} for Arp 244 as a whole (-0.62) is closer to that of CF00 (typical value for local galaxies) than to that of LF17 (-0.48). This suggests that only the Overlap Region (average $n^{\mathrm{ISM}} = -0.45$) exhibits an attenuation curve exponent comparable to $z \sim 2$ (U)LIRGs while the entire system (Arp 244) does not.

Galaxies at $z \sim 2$ observed with ALMA have generally disturbed morphologies with a clumpy dust emission detected at millimetric wavelengths (e.g., Dunlop et al. 2017; Elbaz et al. 2018) that is significantly different and spatially dissociated from that of the stellar populations as derived from the optical bands. We observe the same phenomenon in the Antennae Galaxies, as shown in Fig. 1. SED fitting of these high-z galaxies suggest flatter attenuation curves than that of CF00 ($n^{\mathrm{ISM}} = -0.7$).

Buat et al. (2019) used SED fitting on 17 sources at $z \sim 2$. Six of these galaxies are best fitted with the standard value of

CF00, seven with a Calzetti et al. (2000 hereafter C00) recipe ($n^{\rm ISM} = -0.7$), and the remaining four with a LF17 recipe. Buat et al. (2019) also found that shallow attenuation curves are better suited to describing SEDs of galaxies with a much less extended dust distribution than the light distribution coming from stars.

Pantoni et al. (2021) performed SED fitting on 11 starburst objects at redshift $z \sim 2$ of the GOODS-S field. Nine of these objects are classified as ULIRGs, and the remaining two as LIRGs. Using CIGALE, these authors found that 8 out of their 11 objects are best fitted with a shallower attenuation curve than the standard assumption of $n^{\rm ISM} = -0.7$ (CF00). They obtain a median attenuation curve exponent of $n^{\rm ISM} = -0.5$. which is consistent with the average value we find for the Overlap Region of the Antennae ($n^{\rm ISM} = -0.45$).

Following these comparisons, we observe that high-z galaxies exhibit overall flatter attenuation curves than CF00 while Arp 244 has an attenuation curve close to that of CF00. The Overlap Region is the only part of the system whose attenuation curves resemble the ones found for high-redshift objects.

5.2. Comparison with radiative transfer models

Radiative transfer modelling has been extensively used to study variations of the attenuation curve in both resolved and unresolved galaxies. These studies can be broadly classified into two categories: the first one with dust–stars interactions calculated with several stellar components distributed in bulge and discs (e.g., Silva et al. 1998; Tuffs et al. 2004; Pierini et al. 2004) and the second one relies on hydrodynamical simulations with a post-process radiative transfer analysis (e.g., Saftly et al. 2015; Camps et al. 2016; Feldmann et al. 2017; Rodriguez-Gomez et al. 2019; Roebuck et al. 2019; Trayford et al. 2020). Both predict that the effective attenuation curve depends on the amount of dust attenuation.

5.2.1. Radiative transfer models of low-redshift, resolved galaxies

Using several radiative transfer models for galaxies, Chevallard et al. (2013) proposed a relation (hereafter CH13) linking the slope of the attenuation curve and the optical dust attenuation of the ISM. In Fig. 7, we plot the relation between the V-band attenuation and the exponent of the attenuation curve in the ISM for our 58 regions as well as the CH13 relation.

Overall, the individual regions of Arp 244 follow a similar trend between $n^{\rm ISM}$ and $A_{\rm V}^{\rm ISM}$ to the relation proposed by CH13. Our measured $n^{\rm ISM}$ are found to be higher than the model predictions, inducing flatter curves for a given $A_{\rm V}^{\rm ISM}$, but the large uncertainties on both measurements and model predictions make them at least marginally consistent. Regions associated to NGC 4039 follow the relation more closely than those of NGC 4038, which are scattered in Fig. 7. Regions from the Overlap have, on average, a lower $n^{\rm ISM}$ with respect to the one given by the CH13 relation.

CH13 found that the main drivers of changes in the shape of their optical attenuation curves are the geometry of the dust and the orientation of the galaxy. However, these authors use models of symmetrical, non-perturbed galaxies. While the orientation of NGC 4038 is clearly face-on, orientation is more difficult to assess for the Overlap Region and NGC 4039 as their morphology is very disturbed. These disturbed morphologies and complex dust geometry in the Overlap Region may be what causes these regions to fall outside of the CH13 error margin.

5.2.2. Radiative transfer processing of galaxy formation simulations

In order to simplify the radiative transfer modelling, semi-analytic models of galaxy formation (e.g., Fontanot et al. 2009; Gonzalez-Perez et al. 2013) only provide the basic morphological components of galaxies (bulge and disc) which are in turn modelled using idealised geometries. Thus, it is highly likely that they miss at least part of the influence of multi-scale clumping and inhomogeneity in the galaxy structure. However, hydrodynamical simulations are able to produce structures more representative of real galaxies, such as clumps and inhomogeneities. Targeted hydrodynamical simulations (e.g., Saftly et al. 2015; Feldmann et al. 2017) as well as the more recent hydrodynamical simulations of cosmological volumes (e.g., Camps et al. 2016; Trayford et al. 2020; Rodriguez-Gomez et al. 2019) allow more representative attenuation properties to be produced and compared with observations.

The recent works of Trayford et al. (2020) and Roebuck et al. (2019) give prescriptions on the attenuation curves of high-redshift galaxies which can be compared to our measurements. Using a sample of ∼100 000 simulated galaxies up to $z \sim 2$ from the EAGLE simulations (Schaye et al. 2015; Crain et al. 2015), Trayford et al. (2020) calculated the dust attenuation using the 3D radiative transfer code, SKIRT (Baes et al. 2003, 2011; Camps & Baes 2015). These authors found the same trend as Chevallard et al. (2013): the slope of the attenuation curve $n^{\rm ISM}$ becomes smaller than −0.7 as the optical dust attenuation $A_{\rm V}^{\rm ISM}$ increases. In panel a of Fig. 8, we present our results using bins with a 0.1 mag separation: the slope of the attenuation curve $n^{\rm ISM}$ becomes smaller than −0.7 with increasing optical dust attenuation $A_{\rm V}^{\rm ISM}$. As in Fig. 7, we obtain higher $n^{\rm ISM}$ than the model predictions for a given bin of $A_{\rm V}^{\rm ISM}$.

Trayford et al. (2020) also analysed the possible dependence of the slope of the attenuation curve on the dust surface density. They find that the attenuation curve becomes greyer as the dust surface density increases. Our data for $\Sigma_{\rm dust}$ only range from 5.8 to 6.5 $M_\odot\,{\rm kpc}^{-2}$, (divided into bins separated by 0.1 $\Sigma_{\rm dust}$), but the trend is very similar to the one obtained by Trayford et al. (2020) as shown in panel b of Fig. 8. We also find that regions with $\Sigma_{\rm dust} > 6\,M_\odot\,{\rm kpc}^{-2}$ need a greyer attenuation than the reference value of CF00. The nucleus regions ($\Sigma_{\rm dust}$ bins 6.1 to 6.2 and 6.3 to 6.4 for NGC 4039 and NGC 4038 respectively) correspond to lower values with respect to the model. All the other regions with $\Sigma_{\rm dust} > 6\,M_\odot\,{\rm kpc}^{-2}$ are either inside or adjacent to the Overlap Region. As we find the same trend as Trayford et al. (2020) between $n^{\rm ISM}$ and $\Sigma_{\rm dust}$ but a quite different one between $n^{\rm ISM}$ and $A_{\rm V}^{\rm ISM}$ for low values of $A_{\rm V}^{\rm ISM}$, we conclude that the relation between $\Sigma_{\rm dust}$ and $A_{\rm V}^{\rm ISM}$ is different for the Antennae Galaxies compared to the galaxies from the EAGLE simulations.

Roebuck et al. (2019) used the model library generated by the gadget-2 cosmological N-body/smoothed particle hydrodynamics (SPH) code (Springel 2005). The authors processed these models using the sunrise (Jonsson 2006; Jonsson et al. 2010) radiative transfer suite to generate panchromatic SEDs at 10–100 Myr increments. One feature of interest in Roebuck et al. (2019) is the comparison of the effective attenuation curves of two major merger simulated objects at redshift $z \sim 3$ to several attenuation curve recipes. The two most interesting recipes for

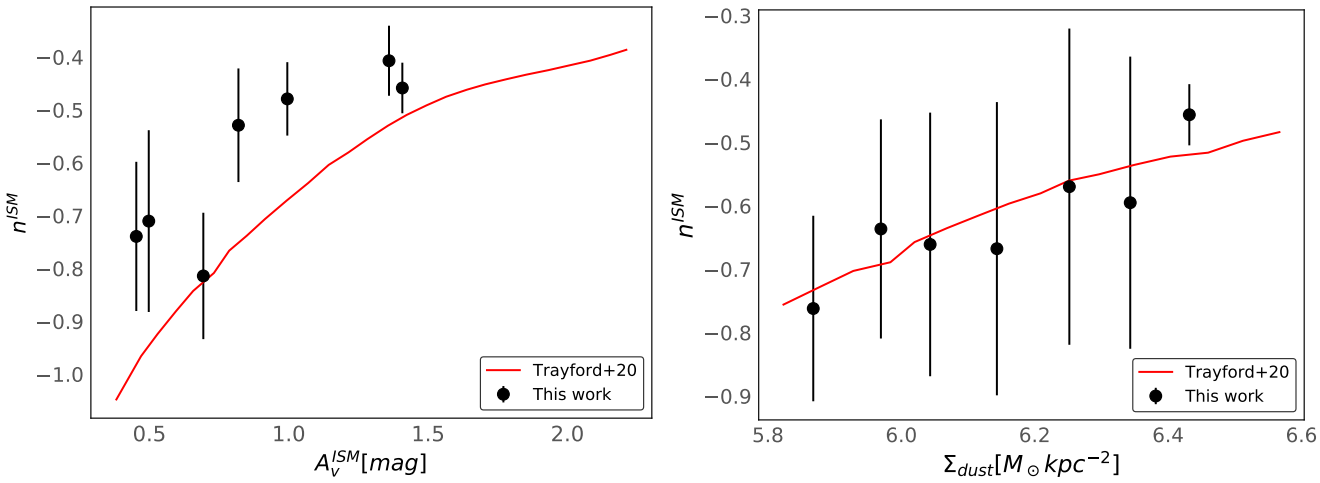

(a) (b)

Fig. 7. Relation between $n^{\rm ISM}$ and dust-associated quantities. The slope of the attenuation curve $n^{\rm ISM}$ is plotted against the optical dust attenuation of the ISM, $A_{\rm V}^{\rm ISM}$, in *panel a* and against the dust surface density, $\Sigma_{\rm dust}$, in *panel b*. The black dots show the mean for each bin (0.1 separation) with its associated error bar. The red curve represents the best fit from Trayford et al. (2020). The mean was only computed if there were more than two objects in the selected bin.

our study are LF17 and C00: the authors plotted different attenuation curves for different epochs of the merger, and show that the more the merger process advances, the steeper the attenuation curve becomes. Up to the coalescence stage, the attenuation curves of both of their mergers is closer to LF17 ($n^{\rm ISM} = -0.48$). However, after the quenching begins, their shape is more similar to that of C00. The epoch marking the coalescence is the one closest to the current state of the Overlap Region. As shown in Fig. 6, the average power law exponent for regions from the Overlap is $n^{\rm ISM} = -0.5$ which is very close to the value from LF17, and in close agreement with the results of Roebuck et al. (2019).

In conclusion, we find that our results for the individual regions of Arp 244 are consistent with the trends set by the models of Chevallard et al. (2013) and Trayford et al. (2020). The same goes for the Overlap Region and the model of Roebuck et al. (2019). However, the whole system of the Antennae is not dominated by this Overlap Region: when we estimate the power-law exponent of the attenuation curve for Arp 244, we find a value close to that found by CF00. Some high-redshift galaxies, such as those observed by ALMA, may share similar properties with an 'extended' Overlap Region.

6. Summary and conclusions

We investigated the reliability of physical parameters estimated with CIGALE by fitting the UV-to-FIR SEDs of 58 regions of the Antennae Galaxies. We used the same configuration for the SFH, dust attenuation, and re-emission for all the regions and the galaxy as a whole. We mapped the spatial distribution of the SFR and the stellar mass, the stellar mass produced during the last burst, the attenuation in the V-band and its power-law slope, and the abundance of PAHs. Our primary findings are as follows:

- We compared the estimates of the physical parameters obtained with the values from 58 regions added together to those obtained for Arp 244 as a whole, and find good agreement, showing that the inability to resolve distant objects does not hinder CIGALE estimations.
- A general flattening of the attenuation curves with increasing attenuation is found, in agreement with radiative transfer modelling; although our measurements correspond to a slightly flatter shape for a given $A_{\rm V}^{\rm ISM}$.
- The attenuation curve recipe proposed by Lo Faro et al. (2017) for high-redshift merger-induced galaxies is the most appropriate to reproduce the SEDs of regions in the Overlap Region. This compatibility is also consistent with the findings of Roebuck et al. (2019) for major mergers up to $z \sim 3$.
- The trend between the slope of the attenuation curve and the dust surface density is in concordance with the findings of Trayford et al. (2020). Similarly, we find that regions with high dust surface density tend to have a shallower attenuation curve than the CF00 value.

From our study of Arp 244, we conclude that the use of a SED fitting tool that preserves the energy balance between stellar and dust emission, such as CIGALE, to measure global physical parameters like the SFR or the stellar mass gives robust results despite the highly inhomogeneous distributions of UV–optical and dust emission across the system.

Acknowledgements. We thank the anonymous referee for her/his very useful comments and suggestions. Médéric Boquien gratefully acknowledges support by the ANID BASAL project FB210003 and from the FONDECYT regular grant 1211000.

References

Allain, T., Leach, S., & Sedlmayr, E. 1996, A&A, 305, 616
Baes, M., Davies, J. I., Dejonghe, H., et al. 2003, MNRAS, 343, 1081
Baes, M., Verstappen, J., De Looze, I., et al. 2011, ApJS, 196, 22
Battisti, A. J., Calzetti, D., & Chary, R. R. 2017, ApJ, 851, 90
Battisti, A. J., Cunha, E. d., Shivaei, I., & Calzetti, D. 2020, ApJ, 888, 108
Bendo, G. J., Galliano, F., & Madden, S. C. 2012, MNRAS, 423, 197
Boquien, M., Buat, V., & Perret, V. 2014, A&A, 571, A72
Boquien, M., Burgarella, D., Roehlly, Y., et al. 2019, A&A, 622, A103
Boquien, M., Buat, V., Burgarella, D., et al. 2022, A&A, 663, A50
Boselli, A., Lequeux, J., & Gavazzi, G. 2004, A&A, 428, 409
Bruzual, G., & Charlot, S. 2003, MNRAS, 344, 1000
Buat, V., Noll, S., Burgarella, D., et al. 2012, A&A, 545, A141
Buat, V., Heinis, S., Boquien, M., et al. 2014, A&A, 561, A39
Buat, V., Boquien, M., Małek, K., et al. 2018, A&A, 619, A135

Buat, V., Ciesla, L., Boquien, M., Małek, K., & Burgarella, D. 2019, A&A, 632, A79
Calzetti, D., Armus, L., Bohlin, R. C., et al. 2000, ApJ, 533, 682
Camps, P., & Baes, M. 2015, Astron. Comput., 9, 20
Camps, P., Trayford, J. W., Baes, M., et al. 2016, MNRAS, 462, 1057
Cardelli, J. A., Clayton, G. C., & Mathis, J. S. 1989, ApJ, 345, 245
Carnall, A. C., McLure, R. J., Dunlop, J. S., & Davé, R. 2018, MNRAS, 480, 4379
Chabrier, G. 2003, PASP, 115, 763
Chambers, K. C., Magnier, E. A., Metcalfe, N., et al. 2016, ArXiv e-prints [arXiv:1612.05560]
Charlot, S., & Fall, S. M. 2000, ApJ, 539, 718
Chevallard, J., Charlot, S., Wandelt, B., & Wild, V. 2013, MNRAS, 432, 2061
Ciesla, L., Charmandaris, V., Georgakakis, A., et al. 2015, A&A, 576, A10
Corre, D., Buat, V., Basa, S., et al. 2018, A&A, 617, A141
Crain, R. A., Schaye, J., Bower, R. G., et al. 2015, MNRAS, 450, 1937
da Cunha, E., Charlot, S., & Elbaz, D. 2008, MNRAS, 388, 1595
Draine, B. T., & Li, A. 2007, ApJ, 657, 810
Draine, B. T., Aniano, G., Krause, O., et al. 2014, ApJ, 780, 172
Dunlop, J. S., McLure, R. J., Biggs, A. D., et al. 2017, MNRAS, 466, 861
Elbaz, D., Leiton, R., Nagar, N., et al. 2018, A&A, 616, A110
Fazio, G. G., Hora, J. L., Allen, L. E., et al. 2004, ApJS, 154, 10
Feldmann, R., Quataert, E., Hopkins, P. F., Faucher-Giguère, C.-A., & Kereš, D. 2017, MNRAS, 470, 1050
Fontanot, F., Somerville, R. S., Silva, L., Monaco, P., & Skibba, R. 2009, MNRAS, 392, 553
Gil de Paz, A., Boissier, S., Madore, B. F., et al. 2007, ApJS, 173, 185
Gómez-Guijarro, C., Toft, S., Karim, A., et al. 2018, ApJ, 856, 121
Gonzalez-Perez, V., Lacey, C. G., Baugh, C. M., Frenk, C. S., & Wilkins, S. M. 2013, MNRAS, 429, 1609
Hodge, J. A., Swinbank, A. M., Simpson, J. M., et al. 2016, ApJ, 833, 103
Jonsson, P. 2006, MNRAS, 372, 2
Jonsson, P., Groves, B. A., & Cox, T. J. 2010, MNRAS, 403, 17
Karl, S. J., Naab, T., Johansson, P. H., et al. 2010, ApJ, 715, L88
Karl, S. J., Lunttila, T., Naab, T., et al. 2013, MNRAS, 434, 696
Kennicutt, R. C., & Evans, N. J. 2012, ARA&A, 50, 531
Klaas, U., Nielbock, M., Haas, M., Krause, O., & Schreiber, J. 2010, A&A, 518, L44
Kriek, M., & Conroy, C. 2013, ApJ, 775, L16
Lahén, N., Johansson, P. H., Rantala, A., Naab, T., & Frigo, M. 2018, MNRAS, 475, 3934
Lo Faro, B., Buat, V., Roehlly, Y., et al. 2017, MNRAS, 472, 1372
Magnier, E. A., Schlafly, E. F., Finkbeiner, D. P., et al. 2020, ApJS, 251, 6
Małek, K., Buat, V., Roehlly, Y., et al. 2018, A&A, 620, A50
McMahon, R. G., Banerji, M., Gonzalez, E., et al. 2013, The Messenger, 154, 35
Mirabel, I. F., Vigroux, L., Charmandaris, V., et al. 1998, A&A, 333, L1
Noll, S., Burgarella, D., Giovannoli, E., et al. 2009, A&A, 507, 1793
Pantoni, L., Lapi, A., Massardi, M., et al. 2021, MNRAS, 504, 928
Pierini, D., Gordon, K. D., Witt, A. N., & Madsen, G. J. 2004, ApJ, 617, 1022
Pilbratt, G. L., Riedinger, J. R., Passvogel, T., et al. 2010, A&A, 518, L1
Privon, G. C., Barnes, J. E., Evans, A. S., et al. 2013, ApJ, 771, 120
Renaud, F., Bournaud, F., & Duc, P.-A. 2015, MNRAS, 446, 2038
Rieke, G. H., Young, E. T., Engelbracht, C. W., et al. 2004, ApJS, 154, 25
Riess, A. G., Macri, L., Casertano, S., et al. 2011, ApJ, 730, 119
Rodriguez-Gomez, V., Snyder, G. F., Lotz, J. M., et al. 2019, MNRAS, 483, 4140
Roebuck, E., Sajina, A., Hayward, C. C., et al. 2019, ApJ, 881, 18
Roussel, H. 2013, PASP, 125, 1126
Rujopakarn, W., Dunlop, J. S., Rieke, G. H., et al. 2016, ApJ, 833, 12
Rujopakarn, W., Daddi, E., Rieke, G. H., et al. 2019, ApJ, 882, 107
Saftly, W., Baes, M., De Geyter, G., et al. 2015, A&A, 576, A31
Salim, S., & Narayanan, D. 2020, ARA&A, 58, 529
Salim, S., Boquien, M., & Lee, J. C. 2018, ApJ, 859, 11
Salmon, B., Papovich, C., Long, J., et al. 2016, ApJ, 827, 20
Sanders, D. B., Mazzarella, J. M., Kim, D. C., Surace, J. A., & Soifer, B. T. 2003, AJ, 126, 1607
Schaye, J., Crain, R. A., Bower, R. G., et al. 2015, MNRAS, 446, 521
Schlafly, E. F., & Finkbeiner, D. P. 2011, ApJ, 737, 103
Silva, L., Granato, G. L., Bressan, A., & Danese, L. 1998, ApJ, 509, 103
Springel, V. 2005, MNRAS, 364, 1105
Tasca, L. A. M., Le Fèvre, O., Hathi, N. P., et al. 2015, A&A, 581, A54
Trayford, J. W., Lagos, C. d. P., Robotham, A. S. G., & Obreschkow, D. 2020, MNRAS, 491, 3937
Tuffs, R. J., Popescu, C. C., Völk, H. J., Kylafis, N. D., & Dopita, M. A. 2004, A&A, 419, 821
Villa-Vélez, J. A., Buat, V., Theulé, P., Boquien, M., & Burgarella, D. 2021, A&A, 654, A153
Whitmore, B. C., & Schweizer, F. 1995, AJ, 109, 960
Zhang, H.-X., Gao, Y., & Kong, X. 2010, MNRAS, 401, 1839

Appendix A: Background noise map

In Fig. A.1 we present the locus of the 66 regions used to compute the background noise in all the images used in this work and listed in Table 1.

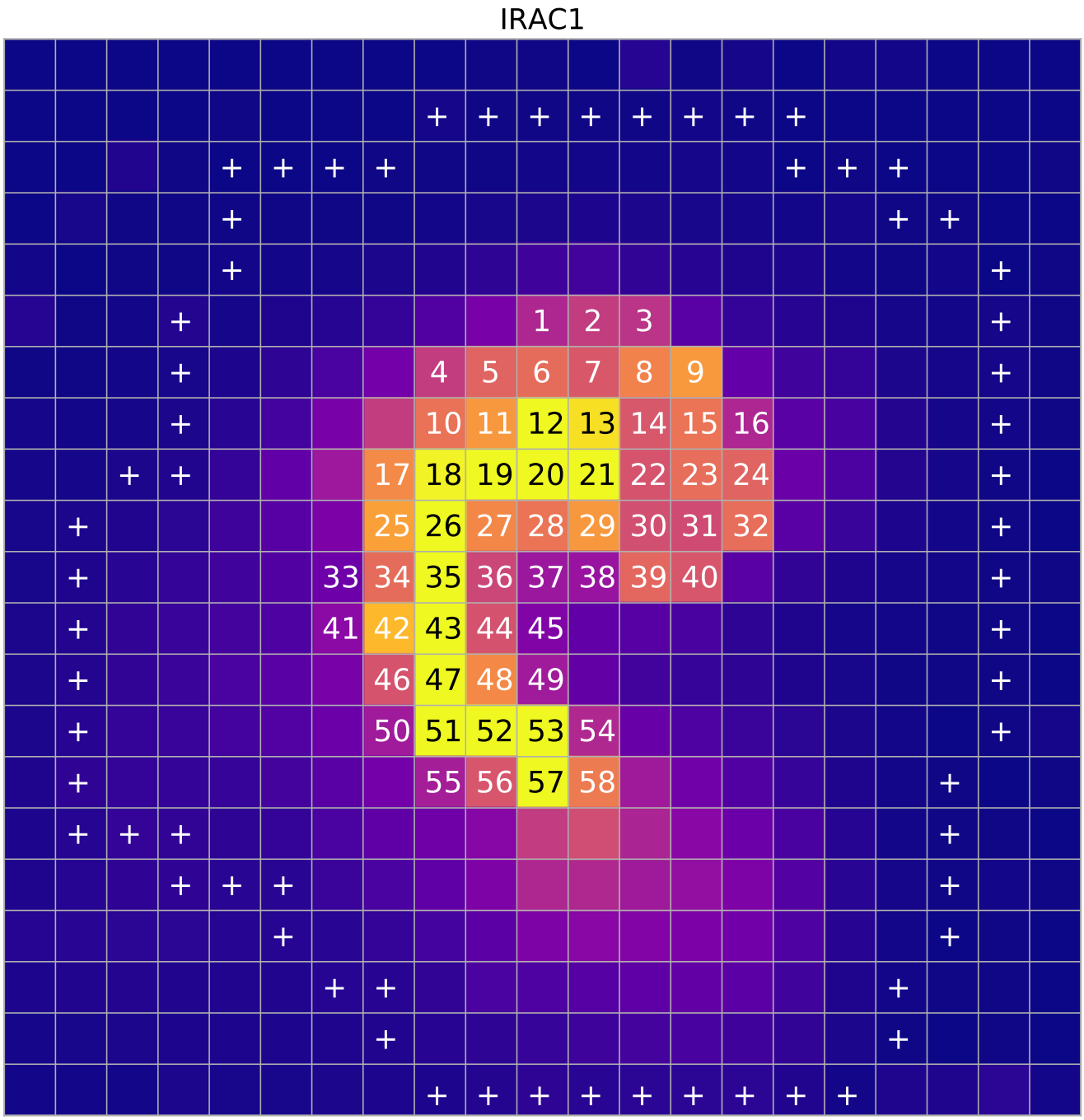

Fig. A.1. The 66 regions used to compute the background noise (marked with white crosses) represented on the IRAC1 band image.